Journal of Inflammation Research

Dovepress
Taylor & Francis Group

Open Access Full Text Article

ORIGINAL RESEARCH

Single-Cell RNA Sequencing Reveals Cellular Heterogeneity and Microenvironmental Remodeling in Human Ureteral Scar Stricture Tissue

Xiaobo Ding[1–4,*], Guoxiang Li[1–3,*], Yuehan Yang[1–3,*], Zhengyao Song[1–3], Xudong Shen[1–3], Bingbing Hou[1–3], Meng Zhang[1–3], Shifang Sang[4], Jian Dai[5], Jiankang Zhang[6], Zongyao Hao[1–3], Yang Chen[1–3], Chaozhao Liang[1–3]

[1]Department of Urology, the First Affiliated Hospital of Anhui Medical University, Hefei, Anhui, People's Republic of China; [2]Institute of Urology, Anhui Medical University, Hefei, Anhui, People's Republic of China; [3]Anhui Province Key Laboratory of Genitourinary Diseases, Anhui Medical University, Hefei, Anhui, People's Republic of China; [4]Department of Urology, Lu'an People's Hospital of Anhui Province, Lu'an, Anhui, People's Republic of China; [5]Department of Otorhinolaryngology, Lu'an People's Hospital of Anhui Province, Lu'an, Anhui, People's Republic of China; [6]Department of Infectious Diseases, Lu'an People's Hospital of Anhui Province, Lu'an, Anhui, People's Republic of China

*These authors contributed equally to this work

Correspondence: Yang Chen, Department of Urology, The First Affiliated Hospital of Anhui Medical University, Jixi Road, Shushan District, Hefei, Anhui, 230022, People's Republic of China, Email douxing20210107@163.com; Chaozhao Liang, Department of Urology, The First Affiliated Hospital of Anhui Medical University, Jixi Road, Shushan District, Hefei, Anhui, 230022, People's Republic of China, Tel/Fax +86 55162922234, Email liang_chaozhao@ahmu.edu.cn

Purpose: This study aimed to construct a comprehensive single-cell transcriptomic atlas of human ureteral scar stricture tissue using single-cell RNA sequencing (scRNA-seq), to uncover cellular heterogeneity, subpopulation dynamics, and intercellular communication networks.

Methods: Ureteral tissues were collected from three normal controls (CTR) and three patients with ureteral scar stricture (US). Single-cell suspensions were prepared using the MobiNova-100 platform and sequenced on the Illumina NovaSeq 6000 system. Data were analyzed using Seurat, Harmony, Monocle2 (for pseudotime trajectory analysis), CellChat (for cell-cell communication), and SCP (for GO/KEGG enrichment). Key findings were validated by multiplex immunofluorescence (IF) and immunohistochemistry (IHC).

Results: Eleven major cell types were identified, including epithelial, stromal, endothelial, and immune cells, each comprising distinct subpopulations. Compared to CTR tissues, US tissues exhibited an increased proportion of $S100A8^+$ and $MT1E^+$ basal epithelial cells with pro-inflammatory characteristics. Fibroblasts displayed substantial heterogeneity, with expansion of inflammatory fibroblasts and smooth muscle cell subsets. Endothelial cells (ECs) showed upregulated inflammatory and antigen presentation pathways. Macrophages exhibited mixed M1/M2 polarization, with enrichment of $APOE^+$ and $APOBEC3A^+$ subsets. Additionally, Th17, Treg, and $CD8^+$ T cell populations were elevated. Cell-cell communication analysis revealed enhanced signaling among fibroblasts, ECs, and immune subsets, particularly via PERIOSTIN, collagen, and laminin pathways.

Conclusion: This study presents the first high-resolution single-cell atlas of ureteral scar stricture tissue, revealing profound cellular heterogeneity and remodeling of the immune–stromal–epithelial landscape. The findings also highlight intensified intercellular communication within the fibrotic microenvironment, offering novel insights into disease pathogenesis and potential therapeutic targets.

Keywords: ureteral stricture, single-cell rna sequencing, cell-cell communication, immune microenvironment

Received: 14 May 2025
Accepted: 28 August 2025
Published: 15 September 2025

Introduction

The ureter is a vital component of the urinary system, responsible for transporting urine from the renal pelvis to the bladder. Structurally, it consists of a multilayered epithelium-comprising basal, intermediate, and umbrella cells—supported by underlying connective tissue, a lamina propria, and a muscularis layer composed of smooth muscle cells and elastic fibers.[1] Disruptions of cellular homeostasis within the ureter can lead to various urological disorders, many of which may progress to ureteral scar stricture.[2,3] Ureteral scar stricture, characterized by luminal narrowing and urinary obstruction, commonly results from trauma, surgical injury, inflammation, ischemia, or neoplastic processes. The central pathological mechanism involves persistent fibrotic remodeling accompanied by local immune dysregulation.[4,5] Although surgical intervention remains the mainstay of clinical management, providing temporary symptom relief and improved urinary drainage, its long-term efficacy is limited, with high rates of recurrence.[5] More critically, there is a lack of effective strategies to halt or reverse fibrotic progression. This therapeutic gap largely stems from an incomplete understanding of the cellular and molecular mechanisms underlying stricture development.

Previous studies have demonstrated that ureteral scar stricture is a chronic and progressive fibrotic disorder, primarily driven by epithelial barrier disruption, aberrant fibroblast activation, immune microenvironmental imbalance, and excessive extracellular matrix (ECM) deposition.[6–8] Under sustained inflammatory stimuli, urothelial cells may undergo epithelial-to-mesenchymal transition (EMT), during which they lose epithelial polarity and cell-cell junctions while acquiring mesenchymal features characterized by α-SMA and vimentin expression. These alterations enhance fibrogenic potential and contribute to tissue stiffening and luminal occlusion.[7,9] Concurrently, fibroblasts differentiate into myofibroblasts, which secrete large quantities of collagen, hyaluronic acid, and fibronectin, exacerbating ECM accumulation and promoting the formation of rigid neotissue. These pathological processes collectively lead to irreversible fibrosis and stricture formation.[10] In addition, aberrant immune cell activation within the local tissue microenvironment plays a pivotal role in coordinating inflammation and fibrogenesis. However, most existing studies have focused on specific signaling pathways, such as TGF-β/Smad, PDGF, and Wnt/β-catenin, or isolated cell populations, lacking a comprehensive understanding of the multicellular interplay and dynamic remodeling events occurring in scarred ureteral tissue.[11,12]

The advent of single-cell RNA sequencing (scRNA-seq) has revolutionized the investigation of cellular heterogeneity and intercellular communication within complex tissues. This high-resolution technique enables the identification of distinct cell subpopulations, transcriptional signatures, developmental trajectories, and cell–cell interaction networks at single-cell resolution. In recent years, scRNA-seq has driven major advances in fibrosis research by uncovering pathogenic cell subsets and key molecular pathways involved in fibrotic progression.[13–16] In urology, single-cell atlases have been successfully constructed for the kidney, bladder, prostate, and urethra, shedding light on organ-specific cellular architecture and immune landscape features.[17–20] However, in the context of ureteral disease, the application of scRNA-seq remains limited, with only a few studies reported to date.[21,22] To our knowledge, no single-cell transcriptomic analyses have been conducted on human ureteral scar stricture under fibrotic pathological conditions.

To address this critical knowledge gap, we performed scRNA-seq on both normal and fibrotic ureteral tissues to generate a comprehensive single-cell transcriptomic atlas. This analysis aimed to identify key cell populations, functional remodeling patterns, and altered intercellular communication networks involved in ureteral scar formation. Special attention was given to characterizing the heterogeneity and dynamic regulatory features of major cell lineages, including epithelial cells, fibroblasts, and immune cells. Through this approach, we identified several potentially pathogenic cell types and signaling pathways that may contribute to the pathogenesis of ureteral scar stricture and represent potential targets for future therapeutic interventions.

Material and Methods

Sample Collection

Tissue specimens were collected from patients undergoing surgery at the Department of Urology, The First Affiliated Hospital of Anhui Medical University, between October 2024 and February 2025. A total of 19 cases were included in the study. Patients were enrolled according to the following criteria: US group: Patients with a history of upper ureteral

calculi who had undergone intracorporeal holmium laser lithotripsy and subsequently developed upper urinary tract obstruction. The diagnosis of upper ureteral stricture was confirmed by imaging examinations (intravenous urography, CT urography, retrograde pyelography, etc.) and ureteroscopic evaluation. All patients underwent laparoscopic resection of the strictured upper ureteral segment followed by urinary tract reconstruction, and postoperative pathology confirmed cicatricial stricture of the upper ureteral lumen. CTR group: Patients who underwent radical nephrectomy, during which normal upper ureteral tissue was obtained intraoperatively, with no tumor invasion into the collecting system. General inclusion criteria: Age ≥18 years; complete clinical data; no prior radiotherapy, chemotherapy, or immunotherapy before surgery. Exclusion criteria: (1) Concomitant urothelial carcinoma or other uncontrolled malignancies; (2) Acute urinary tract infection or systemic infectious diseases with fever; (3) Hematologic disorders or autoimmune diseases; (4) Specimens not meeting the quality control requirements for single-cell RNA sequencing in terms of acquisition or preservation. Among them, 10 patients diagnosed with ureteral scar stricture (US) underwent robot-assisted laparoscopic resection and urinary tract reconstruction. All patients in this group had a history of upper urinary tract stones treated with endoscopic holmium laser lithotripsy. The control group (CTR) consisted of 9 patients with histologically normal ureteral tissues collected during radical nephrectomy for renal tumors without involvement of the collecting system. For scRNA-seq, ureteral tissue samples were collected from three individuals per group (CTR and US). Ethical approval was granted by the Institutional Ethics Committee of The First Affiliated Hospital of Anhui Medical University (Approval No. PJ 2025–02-92). All participants provided written informed consent prior to tissue collection and analysis.

scRNA-Seq Experiment

Immediately after surgical excision, tissue samples were immersed in pre-chilled Hank's Balanced Salt Solution (HBSS; Thermo Fisher Scientific) supplemented with 1% penicillin-streptomycin. Under sterile conditions, tissues were washed three times with ice-cold Dulbecco's phosphate-buffered saline (PBS; Gibco), minced into approximately 1 mm^3 fragments, and washed again with PBS. The minced tissues were transferred into enzyme digestion solution, pre-filtered through a 0.22 μm sterile membrane. Enzymatic digestion was carried out in a 37°C water bath for 30–45 minutes with gentle agitation. Following digestion, the suspension was filtered through a 40 μm nylon mesh to remove debris. The cell suspension was centrifuged at 1,500 rpm for 5 minutes at 4°C. After removing the supernatant, red blood cell lysis was performed using 1 mL RBC Lysis Buffer (Miltenyi Biotec). The cells were then washed twice with PBS and centrifuged again at 1,500 rpm for 5 minutes. Cell viability and concentration were assessed via trypan blue staining (Gibco), ensuring viability exceeded 85%. The cell density was then adjusted to 700–1,200 cells/μL for subsequent scRNA-seq. Single-cell library preparation was conducted using the MobiCube High-throughput Single Cell 3′ Transcriptome Set V2.1 (PN-S050200301) in conjunction with the MobiNova-100 microfluidic platform. Freshly prepared single-cell suspensions were immediately loaded onto microfluidic chips, where automated droplet generation and reagent mixing occurred. Reverse transcription, complementary DNA (cDNA) amplification, and library preparation were performed according to the manufacturer's protocol. Library quality and cDNA concentration were assessed using a Qubit 2.0 Fluorometer (Thermo Fisher Scientific).[23] Final libraries were sequenced on the Illumina NovaSeq 6000 platform using a paired-end 150 bp (PE150) configuration for high-throughput sequencing.

Quality Control, Analysis, and Annotation of scRNA-Seq Data

Raw sequencing outputs in FASTQ format were initially processed using MobiVision software (version 2.1), a dedicated pipeline developed by MobiGene for quality assessment and preprocessing. This tool automatically extracts cell barcodes and unique molecular identifiers (UMIs) embedded in sequencing reads, facilitating precise quantification of transcript levels at the single-cell resolution. The STARSolo alignment module[24] was employed to align reads to the human reference genome (refdata-gex-GRCh38-2024-A), generating essential quality control metrics, including the number of high-quality cells, median gene count per cell, alignment rate, and sequencing saturation, thereby offering a comprehensive evaluation of library performance and sequencing depth.

Subsequent analyses were conducted using the Seurat package (version 4) in R.[25] Expression matrices were imported and converted into Seurat objects for each individual sample. To ensure data integrity, cells were filtered based on the following exclusion criteria: fewer than 500 or more than 6,000 detected genes, total transcript counts below 1,000,

mitochondrial content exceeding 10%, or ribosomal gene content greater than 40%. Genes expressed in fewer than three cells were also excluded. Each sample was independently normalized using the NormalizeData function, followed by identification of highly variable genes (FindVariableFeatures), data scaling (ScaleData), and principal component analysis (PCA). The top 20 principal components (PCs) were selected for Uniform Manifold Approximation and Projection (UMAP) and initial clustering. To correct for batch effects across datasets, the Harmony algorithm[26] was applied. Clustering and visualization (UMAP and t-SNE) were then re-executed using Harmony-adjusted PCs to ensure coherent integration and accurate biological interpretation. To further improve analytical precision, potential doublets were identified using the DoubletFinder package,[27] which simulated homotypic doublet formation, optimized the pK parameter, and classified doublets. Only confidently classified singlets were retained for downstream analyses. To minimize the impact of ambient RNA contamination on gene expression quantification, the decontX[28] algorithm was applied, and only cells with an estimated contamination level below 15% were preserved to maintain transcriptomic accuracy. Before clustering, cell cycle phase scores were calculated for each cell using canonical S-phase and G2/M-phase gene sets provided in Seurat. These scores were regressed out during data scaling to reduce confounding effects from proliferative variability. PCA, clustering, and UMAP visualization were then re-applied to the corrected dataset. Clustering resolution was optimized by testing a range from 0.1 to 1.5, and clustree analysis was used to assess cluster consistency across resolutions. The resolution producing the most stable hierarchical structure was selected for final cell population annotation. Resulting clusters were assigned based on the seurat_clusters identity class. Metadata, including sample identity (orig.ident) and experimental condition (group), were incorporated to support UMAP visualization and group interpretation. The marker genes used for annotating specific cell types are provided in Supplementary Table S1.

Differential Gene Expression and Functional Enrichment Analysis

To thoroughly investigate the biological properties and functional roles of distinct cellular subsets within ureteral scar stricture tissue, differential gene expression analysis was performed to identify significantly altered genes. Enrichment analyses of these differentially expressed genes (DEGs) were subsequently carried out using Gene Ontology (GO) and the Kyoto Encyclopedia of Genes and Genomes (KEGG) pathway databases. These analyses were implemented via the clusterProfiler module integrated within the SCP platform,[29] enabling detailed characterization of relevant biological processes, molecular functions, cellular components, and signaling pathways involved in disease progression.

Pseudotime Trajectory Analysis

To investigate the dynamic developmental progression of key cell populations involved in scar formation, pseudotime trajectory analysis was performed using the Monocle2 package.[30] Dimensionality reduction was implemented via the DDRTree algorithm, which projects cells into a low-dimensional space and arranges them along a continuous trajectory. This enabled the inference of lineage differentiation directions and the identification of critical branch points. Changes in the expression patterns of transcription factors and signaling pathways were examined along the trajectory to uncover potential regulatory mechanisms underlying cell fate transitions.

Cell-Cell Communication Network Analysis

Intercellular communication was analyzed using the CellChat package, which infers potential ligand–receptor interactions by integrating ligand expression from one cell population with corresponding receptor expression in interacting populations. The compareInteractions function was applied to evaluate the relative interaction strength across different sample groups. Communication networks were visualized using netVisual_heatmap and netAnalysis_signalingRole_heatmap, providing insights into the directionality and intensity of signaling events within the tissue microenvironment.

Immunohistochemistry (IHC) Staining

Ureteral tissue specimens were fixed in paraformaldehyde solution, embedded in paraffin blocks, and processed for histological and immunohistochemical staining. Sections were deparaffinized with xylene and rehydrated through a graded ethanol series. Antigen retrieval was performed via heat-induced epitope retrieval using citrate buffer at

elevated temperatures for 10 min. Endogenous peroxidase activity was quenched by incubating sections in 3% hydrogen peroxide for 20 minutes. Samples were then incubated overnight at 4°C with primary antibodies against pan-cytokeratin (pan-CK), α-smooth muscle actin (α-SMA), and CD45 (Supplementary Table S2), diluted in blocking buffer. Following washes, sections were treated with HRP-conjugated secondary antibodies for 20 minutes, and signals were developed using a diaminobenzidine (DAB) detection kit (RCD002, Huilan Biological Technology, China). Finally, stained sections were digitally scanned using a high-resolution pathology imaging system (Huilanbio, Huilan Biological Technology, China) for subsequent analysis.

Multiplex Immunofluorescence (IF) Staining

For IF analysis, paraformaldehyde-fixed, paraffin-embedded (FFPE) ureteral tissue sections were prepared following procedures consistent with the IHC protocol. Sections were incubated with primary antibodies targeting pan-CK, Vimentin, CD31, CD68, CD86, CD163, and CD3 (Supplementary Table S2) in accordance with standard IHC workflows. Subsequently, multiplex fluorescence-conjugated secondary antibodies were applied and incubated in the dark at room temperature for 1 hour. Fluorescent signals were then acquired using a digital pathology scanner (Huilanbio, Huilan Biological Technology, China). Co-localization patterns and spatial organization of cellular markers were examined to validate the spatial distribution inferred from scRNA-seq data.

Results

Cellular Lineage Mapping and Heterogeneity Profiling of Human Ureteral Scar Stricture Tissue

To comprehensively characterize the cellular landscape and functional remodeling associated with ureteral scar stricture (US), we performed scRNA-seq on ureteral tissue samples from three US patients and three normal controls (CTR). Following rigorous quality filtering (retaining cells with >500 and <6,000 detected genes, >1,000 UMIs, <10% mitochondrial, and <40% ribosomal content) (Supplementary Figures S1–S3), a total of 36,853 high-quality single cells were retained, with an average of approximately 6,100 cells per sample (18,415 from CTR and 18,438 from US) (Figure 1A). Dimensionality reduction using UMAP revealed 11 major cellular lineages (Figure 1B), including epithelial cells, fibroblasts, endothelial cells (ECs), monocytes/macrophages, and T cells, which were further classified into 30 transcriptionally distinct subclusters. Cell proportion analysis (Figure 1C) demonstrated a dramatic reduction in epithelial cells in US tissues (from 94.9% to 18.5%), accompanied by notable increases in fibroblasts (from 3.38% to 9.96%), monocytes/macrophages (from 0.54% to 8.36%), and pericytes (from 0.15% to 10.96%). These findings suggest substantial epithelial loss and enhanced stromal and immune cell infiltration within the fibrotic microenvironment. Lineage identity was confirmed through expression of canonical marker genes (Figure 1D), with EPCAM and KRT8 labeling epithelial cells, VIM and COL1A1 marking fibroblasts, CD68 and CD163 identifying macrophages, and CD3D and CD8A distinguishing T cells. Functional enrichment analysis of lineage-specific DEGs (Figure 1E) revealed that epithelial cells in US tissues were enriched in oxidative phosphorylation and stress-response pathways, including responses to metal ions and interferon signaling. Fibroblasts showed upregulation of genes associated with collagen synthesis, ECM remodeling, and TGF-β signaling, while immune cells exhibited activation of IL-17/TNF inflammatory pathways, antigen presentation, and cytotoxicity-related responses. To corroborate the spatial organization suggested by scRNA-seq, multiplex IF staining was conducted (Figure 1F) using lineage-specific markers (pan-CK, Vimentin, CD68, CD163, CD3, CD86, and CD31). The results revealed a marked reduction in pan-CK^+ epithelial cells, a notable expansion of $Vimentin^+$ fibroblasts, and increased infiltration of $CD68^+$/$CD163^+$ macrophages and $CD3^+$ T cells in US tissues, consistent with transcriptomic observations. Collectively, these results uncover extensive cellular remodeling in ureteral scar stricture, characterized by epithelial depletion and expansion of stromal and immune compartments. The coordinated engagement of multiple lineages underscores a dynamic interplay between structural disruption and immune activation, which may contribute to fibrotic disease progression.

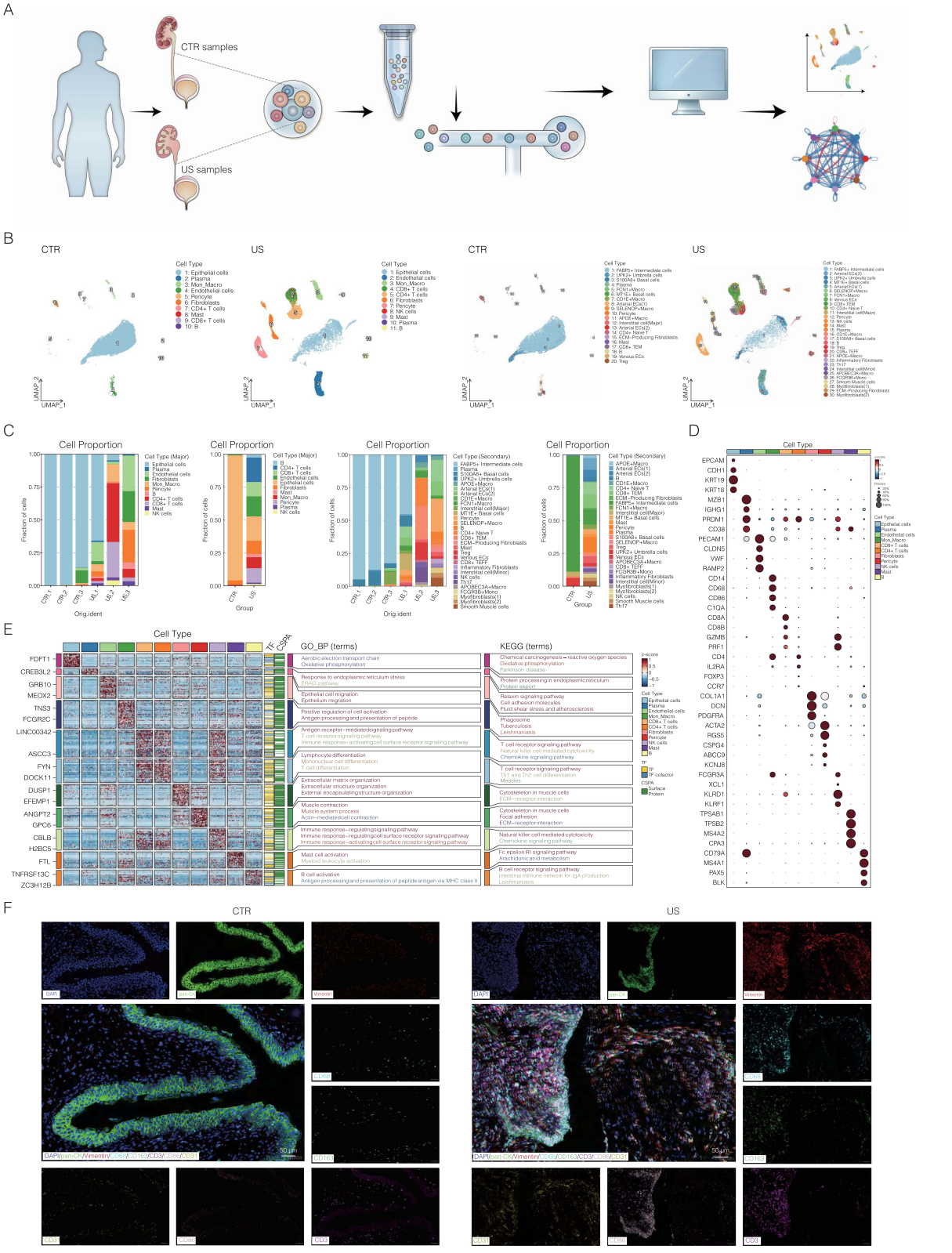

Figure 1 (**A**) Workflow of scRNA-seq analysis. CTR: normal ureter; US: ureteral scar stricture. (**B**) UMAP visualization of cell populations from CTR and US groups after dimensionality reduction. (**C**) Comparative analysis of cellular composition between CTR and US samples. (**D**) Dot plot illustrating the expression patterns of key marker genes across major cell types in the US group. (**E**) DEGs and corresponding functional enrichment analysis of main cell types in the US group. (**F**). Multiplex IF staining (7 markers, 8 colors) validating key cellular subsets and spatial localization.

Single-Cell Characterization of Epithelial Lineages in Ureteral Scar Stricture Tissue

To gain deeper insights into epithelial lineage alterations in ureteral scar stricture, we conducted subclustering analysis of epithelial cells, identifying multiple distinct subpopulations, including mature umbrella cells ($UPK2^+$), intermediate-type cells ($FABP5^+$), and basal-like cells (eg, $KRT5^+$). UMAP projection revealed well-defined clusters corresponding to each subtype, though some subpopulations displayed more diffuse spatial distributions (Figure 2A and B). Compared with the CTR group, epithelial lineages in the US group exhibited pronounced compositional shifts, notably with a significant increase in basal-like cells and a marked decrease in $FABP5^+$ intermediate and $UPK2^+$ umbrella cells (Figure 2C and D). Analysis of marker gene expression demonstrated a striking upregulation of S100A8 and MT1E specifically in US tissues (Figure 2E). Differential expression and heatmap analyses revealed that $FABP5^+$ intermediate and $MT1E^+$ basal cells in US samples expressed numerous genes involved in inflammatory responses, oxidative stress, and immune regulation, whereas $UPK2^+$ umbrella cells were significantly diminished and showed reduced expression of genes associated with barrier maintenance (Figure 2F). GO enrichment analysis further uncovered functional heterogeneity among epithelial subsets (Figure 2G): $FABP5^+$ intermediate cells were enriched in pathways related to immune–metabolic coupling, including fatty acid metabolism and glucocorticoid response; $S100A8^+$ basal cells were associated with interferon signaling and antimicrobial defense; $MT1E^+$ basal cells were linked to metal ion response, cellular stress, and cell–cell adhesion; $UPK2^+$ umbrella cells showed enrichment in steroid and cholesterol biosynthesis, underscoring their role in maintaining epithelial barrier integrity. To explore the developmental dynamics of epithelial cells during fibrosis, we reconstructed pseudotime trajectories using Monocle2 (Figure 2I–K). In the CTR group, cells followed a linear differentiation path from basal to intermediate to mature umbrella states. In contrast, the US group exhibited disrupted differentiation trajectories, with $S100A8^+$, $MT1E^+$, and $FABP5^+$ cells predominantly occupying early pseudotime stages, suggesting impaired maturation or aberrant activation. Meanwhile, $UPK2^+$ umbrella cells were sparse and localized at late pseudotime points, indicating defective terminal differentiation and loss of barrier function. Multiplex IF staining (Figure 2H) further validated transcriptomic observations, revealing significant upregulation of MT1E and S100A8 proteins in the epithelial layer of US tissues, accompanied by a marked reduction in pan-CK^+ epithelial staining. These findings were corroborated by IHC, which also demonstrated reduced pan-CK expression in the US group (Figure 2L), supporting the occurrence of epithelial attrition and enhanced EMT. In conclusion, these results demonstrate that epithelial lineages in ureteral scar stricture tissue undergo profound structural disintegration, developmental impairment, and functional reprogramming. These changes suggest that epithelial cells may serve dual roles, as early victims of barrier breakdown and as active participants in driving inflammation and fibrotic progression.

Single-Cell Characterization of Fibroblast Lineages in Ureteral Scar Stricture Tissue

As central mediators of fibrosis, fibroblasts in ureteral scar stricture (US) tissues were subjected to detailed single-cell analysis. UMAP-based dimensionality reduction identified seven transcriptionally distinct mesenchymal subpopulations (Figure 3A), including inflammatory fibroblasts, ECM-producing fibroblasts, smooth muscle cells (SMCs), and two discrete myofibroblast subsets (Figure 3B). Differential gene expression analysis revealed that fibroblasts in the US group exhibited not only significant alterations in cell-type proportions but also pronounced transcriptional and functional heterogeneity (Figure 3C). Pathway enrichment analysis further uncovered distinct subtype-specific functional programs, encompassing ECM remodeling, inflammatory signaling, actomyosin contractility, and chemokine-mediated pathways (Figure 3D), indicating varied pathological roles across different phases of scar progression. Notably, both ECM-producing fibroblasts and myofibroblast subtypes displayed sustained activation of profibrotic signaling pathways. To investigate fibroblast developmental dynamics, we reconstructed pseudotime trajectories using Monocle2, which revealed a transition from quiescent to activated fibroblast states (Figure 3E). Fibroblasts from the US group were predominantly localized at the terminal ends of the trajectory, suggesting a more mature or activated phenotype (Figure 3F). Integration of subtype identity along the trajectory further demonstrated that ECM-producing fibroblasts and myofibroblasts were significantly enriched at these terminal stages (Figure 3G), underscoring their pivotal roles in late-stage fibrotic remodeling. To validate these transcriptomic findings, multiplex IF and IHC were employed to assess the spatial expression of NRG1 (upregulated in ECM-producing fibroblasts) and α-SMA (a canonical marker of myofibroblasts)

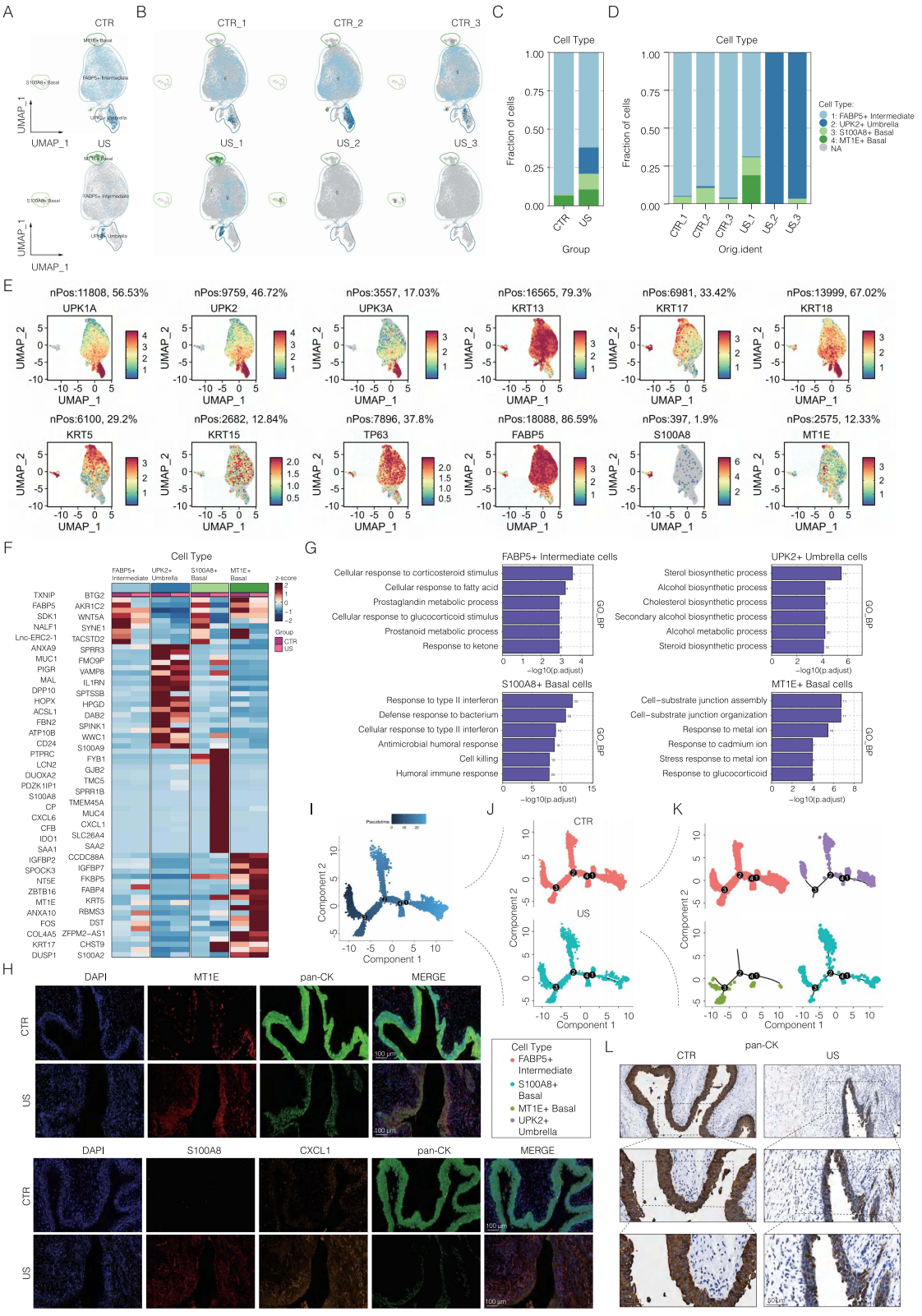

Figure 2 (**A**) UMAP plot of epithelial cells after integration across samples, showing overall cell distribution in two dimensions. (**B**) UMAP plots of epithelial cells from individual samples. (**C**) Bar plot showing the overall proportion of each epithelial cell subtype. (**D**) Bar plot comparing the distribution of epithelial cell subtypes across individual samples. (**E**) Feature plot displaying the expression patterns of epithelial marker genes in CTR and US groups. (**F**) Heatmap of DEGs among epithelial subpopulations in the US group. (**G**) GO enrichment analysis of DEGs in epithelial subpopulations from the US group. (**H**) Multiplex IF staining validating the spatial localization and phenotypic identity of epithelial subtypes. (**I**) Pseudotime trajectory of epithelial cells constructed using Monocle2, illustrating their dynamic transitions. (**J**). Pseudotime trajectory plots comparing epithelial differentiation states between CTR and US groups. (**K**) Spatial distribution of pseudotime states across different epithelial subpopulations. (**L**) IHC staining images validating key molecular features of epithelial cells.

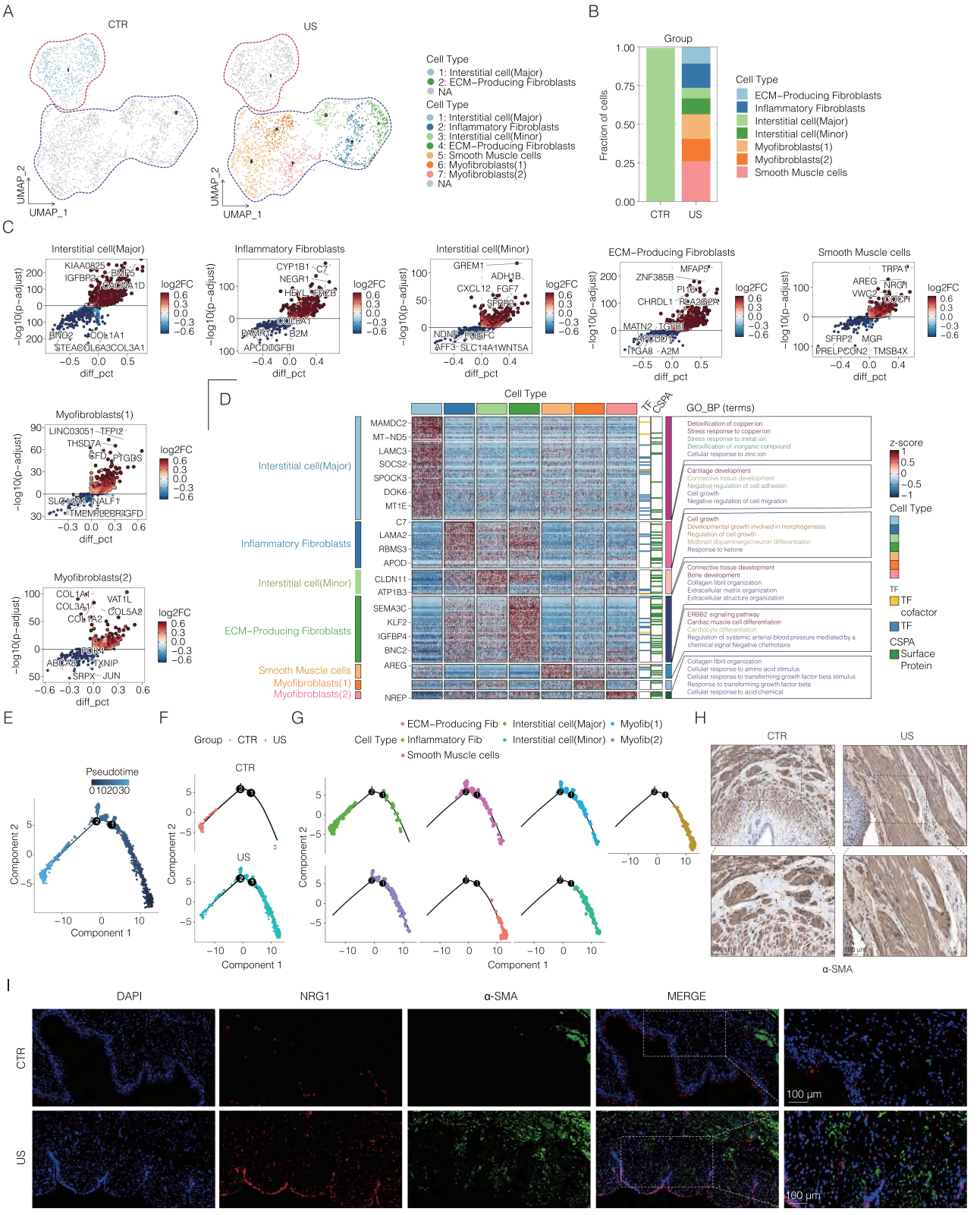

Figure 3 (**A**) UMAP plots displaying the distribution of fibroblasts in the CTR and US groups. (**B**) Bar plots illustrating the proportional distribution of fibroblast subpopulations in CTR and US samples. (**C**) Dot plot showing DEGs among fibroblast subtypes in the US group. (**D**) Heatmap and GO enrichment analysis of DEGs in fibroblast subpopulations from the US group. (**E**) Pseudotime trajectory of fibroblasts reconstructed using Monocle2, illustrating lineage progression. (**F**) Comparative pseudotime trajectory plots of fibroblasts in CTR and US groups, reflecting dynamic transitions. (**G**) Spatial distribution of pseudotime states across distinct fibroblast subpopulations. (**H**). Immunohistochemical staining validating the expression and localization of marker genes in fibroblast subsets. (**I**) Multiplex IF staining demonstrating spatial identity and heterogeneity of fibroblast subpopulations.

https://doi.org/10.2147/JIR.S540340

(Figure 3H and I). In US tissues, NRG1 and α-SMA exhibited overlapping expression patterns within the subepithelial stroma and scar core, confirming their identity as profibrotic fibroblast subsets. Additionally, the distribution of α-SMA provided histological evidence of tissue remodeling. In CTR tissues, α-SMA expression was restricted to the inner longitudinal and outer circular smooth muscle layers, reflecting normal ureteral structure. In contrast, US tissues displayed disorganized expansion of α-SMA cells within the inner muscle layer, accompanied by extensive immune infiltration (Figure 3H), suggesting a convergence of structural disarray and inflammatory activation during fibrotic progression. Collectively, fibroblasts in ureteral scar stricture tissue exhibit pronounced functional heterogeneity and divergent developmental trajectories. Among these, ECM-producing fibroblasts and myofibroblasts emerge as dominant profibrotic populations driving advanced tissue remodeling, thereby representing promising therapeutic targets for anti-fibrotic intervention.

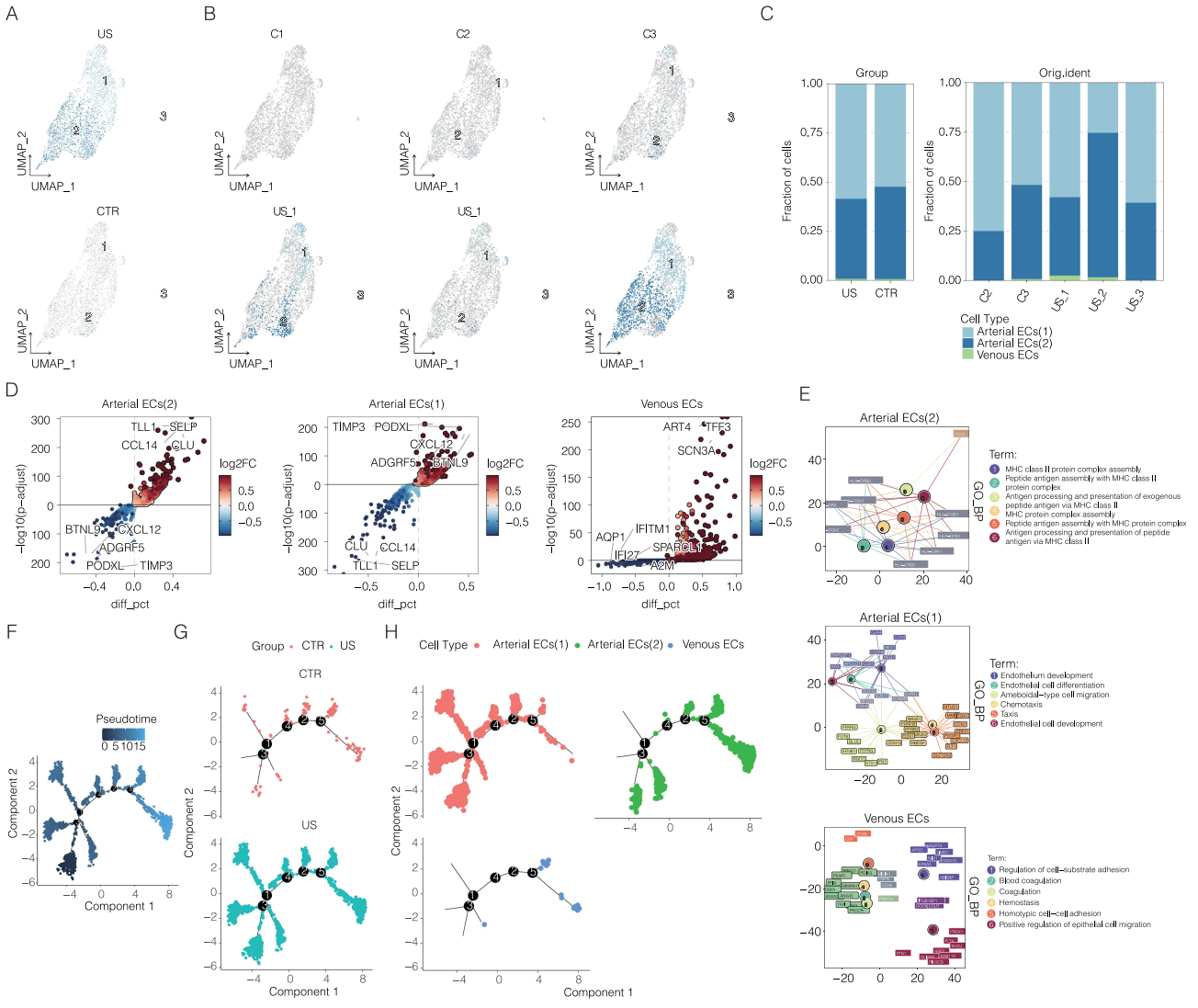

Figure 4 (**A**) UMAP clustering of ECs in the CTR and US groups. (**B**). UMAP plots showing the distribution of ECs across individual samples in the CTR and US groups. (**C**) Bar plots comparing the proportional composition of endothelial cell subtypes between CTR and US groups. (**D**) Differential gene expression analysis of endothelial cell subtypes in the CTR and US groups. (**E**) GO enrichment analysis of biological processes in different endothelial subtypes from the US group. **(F)** Pseudotime trajectory of ECs constructed using Monocle2, reflecting developmental progression. (**G**) Comparative pseudotime trajectory plots of ECs in the CTR and US groups. (**H**) Spatial distribution of pseudotime states across distinct endothelial cell subpopulations.

Single-Cell Characterization of ECs in Human Ureteral Scar Stricture Tissue

To examine transcriptional alterations in ECs within ureteral scar stricture (US) tissue, we conducted UMAP-based clustering analysis of EC populations from both CTR and US groups, identifying several functionally distinct subtypes. Notably, Arterial ECs(1) were markedly expanded in the US group, while Venous ECs were nearly absent (Figure 4A–C). Differential gene expression analysis revealed that Arterial ECs(2) upregulated genes related to inflammation and cell adhesion, while genes involved in vascular homeostasis were downregulated. In contrast, Arterial ECs(1) exhibited elevated expression of CXCL12 and PODXL, along with reduced expression of inflammatory markers, suggesting a role in vascular stability maintenance. In Venous ECs, upregulated genes such as SPARCL1, SCN3A, and TFPI indicated potential involvement in cell-matrix interactions and vascular function regulation (Figure 4D). GO enrichment analysis further delineated the functional heterogeneity among EC subsets (Figure 4E). Arterial ECs(2) were enriched in immune-related pathways, including antigen presentation and T cell activation, whereas Arterial ECs(1) were primarily associated with vascular development, cell migration, and structural integrity. Venous ECs demonstrated significant enrichment in pathways related to cell-matrix adhesion, coagulation regulation, and epithelial migration, suggesting a potential role in tissue repair and microvascular remodeling. To investigate the dynamic transcriptional changes of endothelial lineages, we performed pseudotime trajectory analysis using Monocle2 (Figure 4F). ECs from the US group were broadly distributed along the trajectory, with a pronounced accumulation at the terminal state, indicating a shift toward late-stage differentiation or activation (Figure 4G). Cell subtype mapping revealed that Arterial ECs(1) were localized at early pseudotime stages, while Arterial ECs(2) and Venous ECs were predominantly situated at intermediate and late stages, respectively (Figure 4H). Collectively, these results demonstrate that ECs in ureteral scar stricture tissues undergo substantial lineage restructuring and transcriptional reprogramming. Arterial ECs(2) and Venous ECs exhibit signatures of inflammatory activation and enhanced adhesion, implicating them in pathological vascular remodeling and immune-mediated processes during scar stricture progression.

Single-Cell Characterization of Macrophages in Human Ureteral Scar Stricture Tissue

To explore the lineage heterogeneity and immune functional states of macrophages in ureteral scar stricture (US) tissues, we performed reclustering analysis of $CD68^+$ cells from the US group. UMAP visualization revealed six transcriptionally distinct macrophage subsets with diverse functional profiles, including $APOE^+$, $APOBEC3A^+$, $CD1E^+$, $SELENOP^+$, and $FCN1^+$ macrophages, as well as $FCGR3B^+$ monocytes (Figure 5A and B). Among these, $APOBEC3A^+$ and $FCGR3B^+$ subsets were significantly enriched in US tissues, suggesting a potential role in the fibrotic microenvironment. Each subset exhibited a distinct gene expression signature (Figure 5C). Proinflammatory genes such as IL1B, CD86, and STAT1 were predominantly expressed in M1-like macrophages, while immunoregulatory genes including MRC1 and CD163 were enriched in M2-like subsets, indicating the coexistence of M1 and M2 polarization states within the fibrotic niche. Polarization scoring further revealed spatial heterogeneity across the UMAP landscape: M1-polarized macrophages were enriched in the upper left region, whereas M2-associated features were concentrated in the lower right (Figure 5D). Differential gene expression analysis identified subset-specific marker genes (Figure 5E), and functional enrichment analysis revealed their putative immune roles (Figure 5F): $SELENOP^+$ macrophages were linked to metal ion homeostasis and antioxidant defense; $APOBEC3A^+$ macrophages were enriched in pathways related to antigen presentation and T cell activation; $FCN1^+$ cells showed enrichment in chemokine signaling and bacterial defense responses, implicating them in innate immune activation. Pseudotime trajectory analysis using Monocle2 revealed that macrophages from US tissues were predominantly distributed at both the initial and terminal stages of the developmental trajectory (Figure 5G). Dynamic gene expression profiling along the pseudotime axis demonstrated sustained upregulation of immune regulators such as CCL18 and CXCL9, indicative of macrophage participation in chronic inflammation and immune modulation (Figure 5H). To validate the transcriptomic results, multiplex IF staining confirmed the spatial accumulation of $APOE^+$ macrophages within the subepithelial stroma of US tissues, co-expressing MMP19 and CD11B (Figure 5I). These findings suggest that $APOE^+$ macrophages may contribute to ECM degradation and cell migration, thereby playing a crucial role in tissue remodeling and scar formation. In summary, these data reveal profound functional

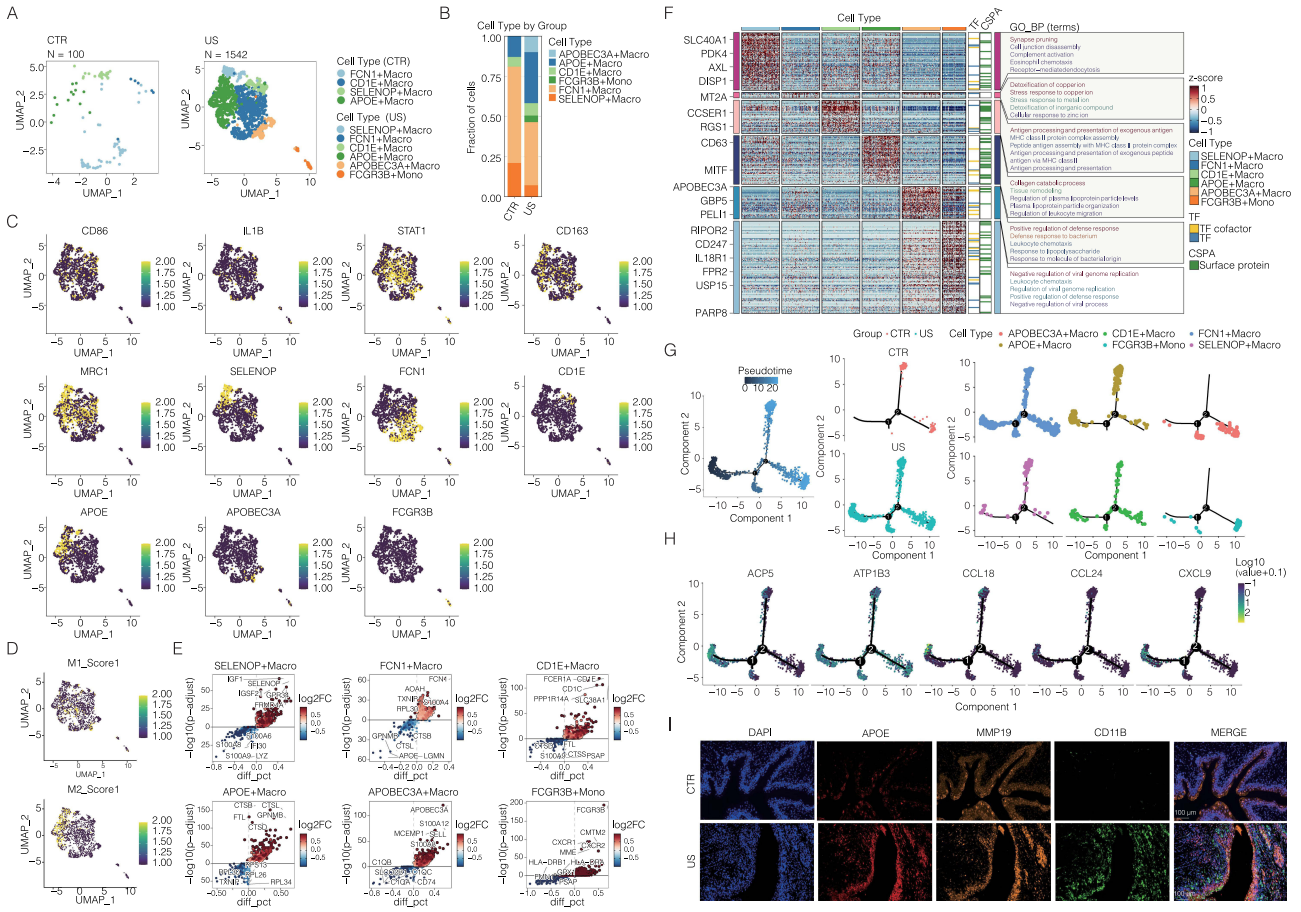

Figure 5 (**A**) UMAP plot showing the distribution of macrophage subpopulations in the CTR and US groups. (**B**) Bar plots illustrating the proportional composition of macrophage subsets in the CTR and US groups. (**C**) UMAP expression maps of functional state-related genes in macrophages from the US group. (**D**) UMAP visualization of M1/M2 polarization scores in macrophages within the US group. (**E**) Differential expression analysis of macrophage subpopulations in the US group. (**F**) Transcriptional profiling and functional pathway enrichment analysis of macrophage subtypes in the US group. (**G**) Pseudotime trajectory plots depicting the overall and subset-specific differentiation paths of macrophages. (**H**) Dynamic expression profiles of key genes along the pseudotime trajectory in US-derived macrophages. (**I**) Multiplex IF validation images of macrophage marker expression and localization.

heterogeneity and terminal pro-inflammatory polarization of macrophages in ureteral scar stricture, underscoring their central role in immune regulation and fibrotic tissue remodeling.

Single-Cell Resolution Reveals T Cell Heterogeneity and Immune Activation in Ureteral Scar Tissue

To comprehensively characterize the compositional dynamics and functional reprogramming of T cells within the ureteral fibrotic microenvironment, we conducted UMAP-based clustering, identifying six transcriptionally distinct T cell subsets with functional heterogeneity: $CD4^+$ naive T cells, $CD8^+$ effector memory T cells ($CD8^+$ TEM), $CD8^+$ activated effector T cells ($CD8^+$ TEFF), Th17 cells, regulatory T cells (Tregs), and NK-like T cells (Figure 6A). In the US group, overall T cell abundance was elevated, accompanied by a substantial shift in subset distribution, marked by increased proportions of $CD8^+$ TEFF, Th17, and Treg cells, alongside a notable depletion of $CD4^+$ naive T cells (Figure 6B). Marker gene analysis revealed distinct transcriptional signatures across T cell subsets (Figure 6C): CD3D and CD3E were broadly expressed across all T cells, while FOXP3 and IL2RA specifically identified Tregs. Th17 cells were characterized by high expression of IL17A, RORC, and CCR6, whereas $CD8^+$ T cell subsets were defined by CD8A, CD8B, GZMK, and TBX21. Heatmap visualization of DEGs further confirmed the functional specialization of each subset (Figure 6D): $CD8^+$ TEFF cells were enriched in cytotoxic activity and T cell activation pathways, Tregs were associated with immunosuppressive signaling, and Th17 cells exhibited elevated expression of pro-inflammatory cytokines and

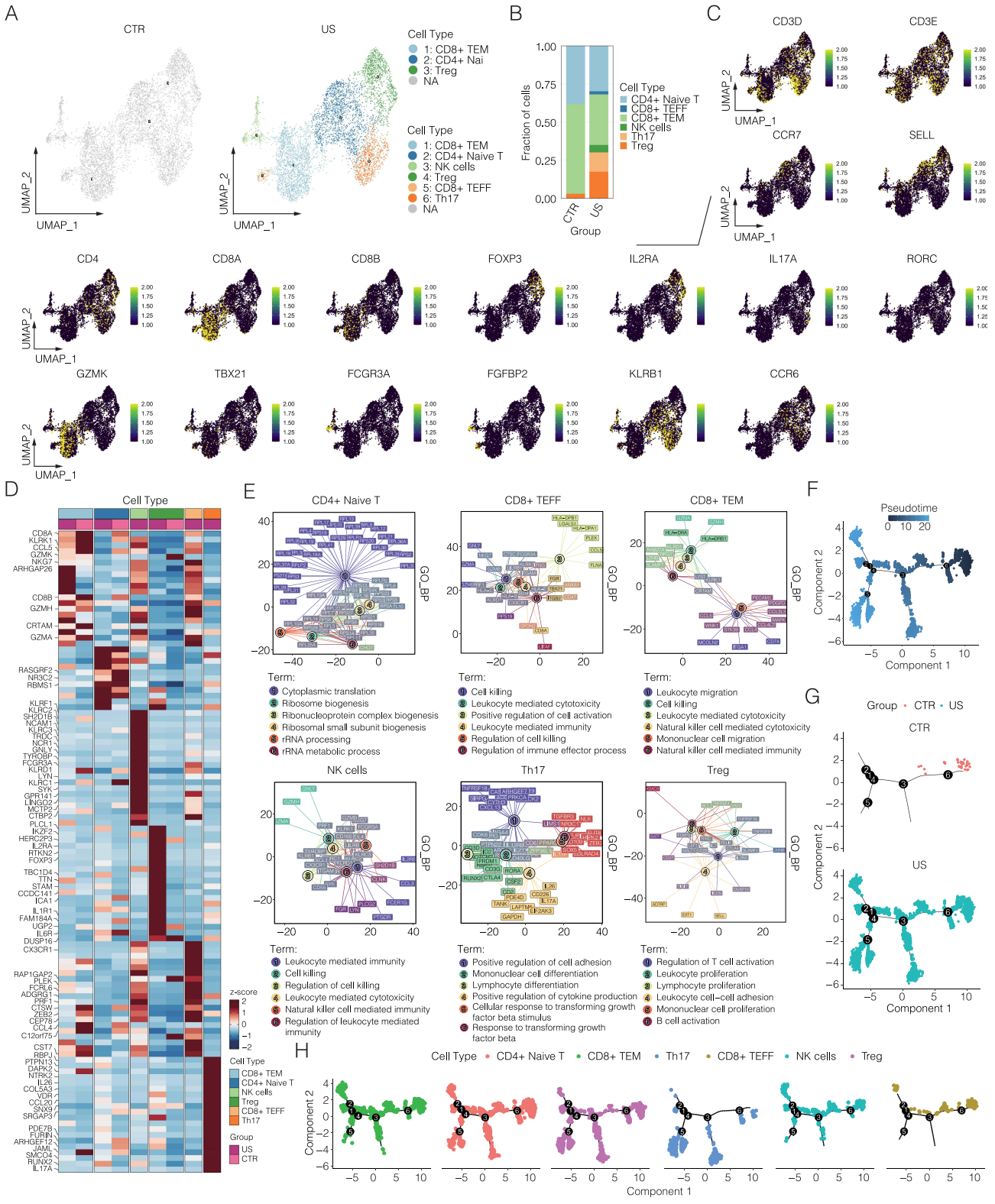

Figure 6 (**A**) UMAP plot depicting the distribution of T cell subpopulations in the CTR and US groups. (**B**) Bar plots showing the proportional composition of T cell subsets in the CTR and US samples. (**C**) UMAP expression plots of key marker genes across T cell subsets in the US group. (**D**) Heatmap analysis of DEGs among T cell subpopulations in the US group. (**E**) GO enrichment analysis of biological processes in US-derived T cell subtypes. (**F**) Pseudotime trajectory of T cells reconstructed using Monocle2, indicating lineage dynamics. (**G**) Visualization of pseudotime trajectories comparing T cell distribution patterns between CTR and US groups. (**H**) Spatial mapping of T cell subpopulations along the pseudotime trajectory.

https://doi.org/10.2147/JIR.S540340

chemotactic mediators. GO enrichment analysis revealed distinct functional roles among T cell subsets, including immune regulation, cytolytic function, and cell adhesion (Figure 6E). Pseudotime trajectory analysis (Figure 6F–H) uncovered complex developmental branching within the US group, with broader cellular dispersion and increased trajectory bifurcation. $CD4^+$ naive T cells were primarily located at the root of the trajectory, while Th17, Treg, and $CD8^+$ TEFF cells were enriched along terminal branches, suggesting a progressive transition from naive to activated or regulatory phenotypes. This dynamic trajectory implies that T cells undergo significant lineage remodeling under fibrotic stress and may function as key modulators of chronic inflammation and immune architecture reorganization during ureteral scar formation.

Intercellular Communication Landscape Across Cell Types in Human Ureteral Scar Tissue

To systematically investigate intercellular communication dynamics in ureteral scar tissue, we employed CellChat to compare signaling networks between the CTR and US groups. The analysis revealed a marked increase in both the total number of inferred interactions (2,833 vs 1,151) and the overall communication strength (68.004 vs 45.009) in the US group, indicating significantly enhanced cellular crosstalk within the fibrotic microenvironment (Figure 7A). Network topology visualization demonstrated that interactions among fibroblasts, epithelial cells, and monocyte/macrophage populations were especially prominent in the US group, forming a central communication hub (Figure 7B). Pathway-level analysis showed that fibrosis-associated signaling pathways, including TGF-β, CD40, WNT, and CSF, were significantly enriched in the US group, whereas the CTR group exhibited dominance of homeostasis-related pathways, such as IL-1, IFN-γ, and EGF (Figure 7C). Signal directionality analysis further revealed that in the US group, fibroblasts, ECs, epithelial cells, and pericytes primarily functioned as signaling sources, while $CD8^+$ T cells and macrophages acted as major signal receivers (Figure 7D). These findings suggest that in fibrotic scar tissue, structural and stromal cells not only provide ECM components but also function as active hubs for immune modulation. Focusing on fibroblast-derived signals, we observed that fibroblasts from US tissues exhibited increased output of signaling pathways associated with ECM remodeling, inflammatory regulation, and cellular stress responses (Figure 7E), underscoring their regulatory prominence and network centrality. To further dissect the role of ECM–integrin signaling in intercellular communication, we analyzed the expression of PERIOSTIN (POSTN) and its major integrin receptors (ITGAV, ITGB5, ITGB3) across cell types (Figure 7F). POSTN was predominantly upregulated in US fibroblasts, while its receptors were broadly expressed in $CD4^+$ T cells and macrophages, indicating a bridging function between the ECM and immune signaling. Similarly, collagen family members (eg, COL1A1, COL1A2, COL6A1) were significantly elevated in fibroblasts, whereas their cognate integrin receptors (ITGA1, ITGA2, ITGB1) were expressed in immune cells, epithelial cells, and pericytes (Figure 7G), supporting a "structural cell output–immune cell response" communication model in fibrosis. In addition, laminin components (eg, LAMA2, LAMB1, LAMB2, LAMC1) and their respective receptors (ITGA6, ITGB1, DAG1) displayed cell type–specific expression patterns, with ligands elevated in fibroblasts and epithelial cells, and receptors upregulated in immune and perivascular cells (Figure 7H), suggesting a role in cell adhesion and spatial tissue organization in fibrotic regions. Collectively, these findings identify fibroblasts in US tissues as central signaling nodes actively orchestrating cell–matrix, immune–matrix, and structural–functional coupling within the fibrotic communication network. This highlights a coordinated, multi-lineage mechanism by which extensive intercellular interaction drives fibrotic scar formation.

Discussion

This study provides the first single-cell transcriptomic profiling of human ureteral scar stricture tissue, revealing the cellular composition and functional states of the lesion. The findings uncover pronounced cellular heterogeneity and complex interactions among epithelial, stromal, endothelial, and immune cell populations within the fibrotic microenvironment. Collectively, the results suggest that ureteral scar formation is orchestrated by a multicellular network involving epithelial barrier dysfunction, stromal activation, immune dysregulation, and the remodeling of ECM-centered signaling pathways.

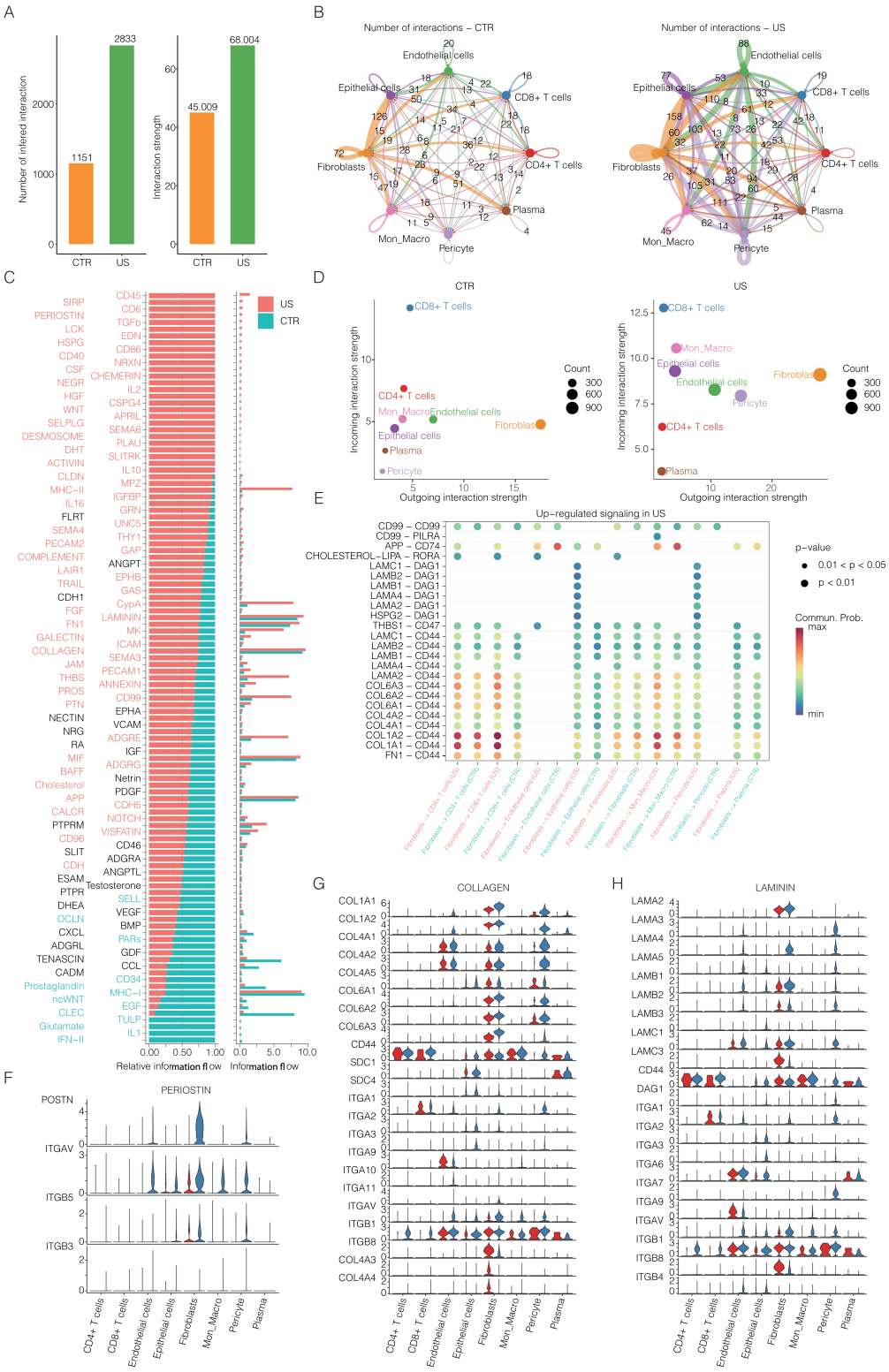

Figure 7 (A) Bar plots comparing the number and overall strength of intercellular communications in the CTR and US groups. (**B**) Reconstructed intercellular communication network in the US group, visualizing major signaling interactions. (**C**) Information flow analysis of signaling pathways between CTR and US groups, highlighting changes in communication intensity. (**D**) Quantitative analysis of incoming and outgoing signaling strength across different cell types in CTR and US samples. (**E**) Analysis of fibroblast-related ligand–receptor signaling pathways significantly upregulated in the US group. (**F**) Expression profiles of PERIOSTIN and its integrin receptors across various cell types. (**G**) Expression patterns of the COLLAGEN family and their integrin receptors across different cell populations. (**H**) Expression maps of the LAMININ family ligands and their corresponding receptors in diverse cell types.

https://doi.org/10.2147/JIR.S540340

Loss of epithelial barrier integrity and abnormal differentiation are considered pivotal in driving fibrotic progression.[31] In ureteral scar stricture tissues, we observed a marked depletion of $UPK2^+$ umbrella cells and a concomitant expansion of $FABP5^+$ intermediate and $S100A8^+$ basal-like epithelial populations, indicating a disrupted regenerative process and potential reprogramming of differentiation trajectories. GO analysis revealed that $FABP5^+$ cells were enriched in pathways related to fatty acid metabolism and the glucocorticoid response, whereas $S100A8^+$ cells upregulated inflammation-associated programs, including type II interferon signaling and cytotoxic immune responses. These results indicate pathological epithelial remodeling under chronic inflammatory stress, mirroring the loss of umbrella cells and disrupted adhesion molecule expression reported in radiation-induced cystitis.[32] We also identified a subset of $MT1E^+$ basal-like cells exhibiting signs of expansion, with gene enrichment pointing to metal ion stress responses and collagen regulation pathways. Combined with IF data, these findings support the spatial localization of MT1E and S100A8 in scar regions and suggest that these cells may be undergoing early stages of EMT. This is consistent with the reported role of EMT in fibrosis across multiple organ systems, including the lung, liver, kidney, and gastrointestinal tract.[33–36] Interestingly, in our previous single-cell study on prostate cancer metabolism, we also identified EMT-related signatures within the tumor microenvironment.[37] Mechanistically, this transition may be initiated by pro-inflammatory cytokines such as IL-1β and TNF-α, and subsequently amplified by TGF-β family members, establishing a self-sustaining inflammation–fibrosis loop.[38] Collectively, these results suggest that epithelial lineage cells are not merely passive targets of injury but actively contribute to tissue remodeling as key modulators of the fibrotic microenvironment.

Fibroblasts constitute the most abundant stromal cell population in scar tissue and are primarily responsible for ECM synthesis and maintenance, thereby playing a central role in tissue repair and wound healing.[39–41] In our study, fibroblasts exhibited pronounced lineage heterogeneity and functional specialization. We identified several transcriptionally distinct subsets, including ECM-producing fibroblasts, myofibroblasts (types 1 and 2), and smooth muscle-like fibroblasts, all of which were markedly expanded in scar tissue samples. These subsets were enriched for pathways involved in collagen biosynthesis, cellular stress response, contractile migration, and growth factor regulation, suggesting their roles in structural remodeling, immune modulation, and chronic inflammation. Notably, the myofibroblast (2) subset expressed hallmark genes associated with activation and contractility, including JUN, PDK4, and COL1A1, exhibiting molecular characteristics highly consistent with pathogenic fibroblast populations observed in dermal scarring, pulmonary fibrosis, and liver cirrhosis.[42–44] These cells may originate from homeostatic fibroblasts undergoing activation in response to local cues such as TGF-β and PDGF, representing a transition toward a "pathologically activated lineage." Pseudotime trajectory analysis using Monocle2 revealed a clear developmental shift, indicating a directional transition from quiescent fibroblasts toward ECM-producing and contractile myofibroblast phenotypes. This finding supports a model of functional chemotaxis underlying scar formation. Integration with macrophage- and T cell-derived signaling further implicated immune–stromal communication, particularly involving TGF-β, IL-6, and OSM, as potential drivers of fibroblast lineage remodeling.[45,46] To confirm the tissue-level expression of key fibroblast markers identified through scRNA-seq, multiplex IF staining was performed for Neuregulin-1 (NRG1) and α-SMA, a well-established myofibroblast marker. The results demonstrated clear co-localization of NRG1 and α-SMA within fibroblast populations enriched in scar tissue, supporting the notion that NRG1 contributes to fibroblast activation and fibrogenesis. These findings are consistent with previous reports in cutaneous fibrosis models,[42] providing strong histological evidence for NRG1 as a regulatory mediator in ureteral fibrotic remodeling.

Macrophages, as principal immune effectors in ureteral scar lesions, exhibited notable lineage complexity and activation diversity. Subtype-specific marker analysis revealed significant upregulation of M1-associated genes, including CD86, IL1B, and STAT1, indicating a substantial skew toward a pro-inflammatory phenotype likely involved in cytokine amplification and pathological immune activation.[47] Concurrently, detectable expression of M2-associated markers such as CD163 and MRC1 suggested the presence of a regulatory macrophage subset, reflecting the functional plasticity of macrophages in fibrotic environments. Notably, the $SELENOP^+$, $APOE^+$, and $FCN1^+$ macrophage subsets were highly enriched in scar tissue. Among them, $APOE^+$ macrophages displayed dual functionality: producing pro-inflammatory mediators while also demonstrating pathway enrichment related to metal ion (zinc and copper) homeostasis, lipid metabolism, and chemotactic signaling. These features implicate $APOE^+$ macrophages in both immune modulation

and tissue remodeling, mirroring their roles in early-stage fibrosis of the liver, lung, and kidney.[48–51] Further evidence from M1/M2 polarization scoring confirmed a dominant M1-type inflammatory profile, though a subset of macrophages exhibited transcriptional characteristics aligned with M2-like reparative activity. This mixed activation landscape supports the concept of dual-function macrophages that simultaneously sustain chronic inflammation and promote tissue repair, in line with the "biphasic immune regulation" model described in various fibrotic pathologies.[52] Pseudotime trajectory reconstruction revealed dynamic transitions across six major macrophage subtypes, suggesting that scar-associated macrophages undergo divergent lineage trajectories to cooperatively mediate inflammatory amplification and immuno-microenvironment remodeling. These transcriptional insights were validated by multiplex IF, which confirmed the spatial enrichment of $APOE^+$ macrophages in fibrotic regions, co-expressing MMP19 and CD11b, markers indicative of roles in ECM remodeling and cell adhesion. Together, these findings underscore $APOE^+$ macrophages as key contributors to fibrotic progression and highlight their therapeutic potential in the context of ureteral scar stricture.

T cells, as key regulators of adaptive immunity, exhibited notable subset remodeling within ureteral scar tissue. A significant enrichment of Th17 and regulatory T cell (Treg) populations was observed, alongside a marked reduction in $CD4^+$ naïve T cells, indicating a shift from immune homeostasis toward chronic activation. Th17 cells, characterized by elevated expression of IL17A, RORC, and CCR6, were enriched in pathways related to TGF-β signaling, cell adhesion, and chemotaxis, implicating them as potential drivers of inflammatory fibrosis. These observations are consistent with the pathogenic roles attributed to Th17 cells in pulmonary fibrosis and Crohn's disease-associated intestinal strictures.[53,54] Treg cells, defined by expression of FOXP3 and IL2RA, exhibited a classic immunosuppressive phenotype and were predominantly localized at the terminal end of the pseudotime trajectory, suggesting involvement in immune resolution and tissue repair during late-stage fibrosis. However, Tregs may also promote fibrogenesis through TGF-β secretion, thereby inducing fibroblast activation and ECM deposition, reflecting a dual role in both immunoregulation and fibrotic progression.[55] Robust upregulation of FOXP3 and IL2RA further confirmed the identity and functional relevance of these cells within the fibrotic niche. Their late-stage positioning in pseudotime supports their role in immune suppression, yet their fibrosis-promoting potential, via cytokine-mediated fibroblast crosstalk, warrants further investigation, particularly in relation to their dynamic interactions with macrophages and epithelial cells.

Cell–cell communication analysis revealed a substantial increase in both the number and strength of intercellular interactions in ureteral scar tissue. Fibroblasts emerged as central signaling hubs, engaging extensively with epithelial and immune cells through key profibrotic pathways, including TGF-β, CD40, and WNT signaling axes, corroborating observations from other fibrotic models.[45,56,57] Upregulation of ECM-related ligand–receptor pairs, such as FN1–CD44 and LAMB2–DAG1, highlighted the critical role of ECM–cell interactions in scar formation, paralleling findings in pulmonary and tubulointerstitial fibrosis, and emphasizing the active role of structural signals in disease pathology.[58,59] Additionally, immune-derived signaling molecules, MIF, IL-1, and CD99, were found to be hyperactivated in fibrotic tissue. These ligands originated primarily from macrophages and $CD8^+$ T cells, while their corresponding receptors were predominantly expressed by fibroblasts, suggesting a directional immune–stromal communication axis. This interaction pattern aligns with the pro-inflammatory and profibrotic roles of MIF in pulmonary fibrosis and IL-1 in renal interstitial fibrosis.[60–63] Such remodeling of the signaling network reflects the pathophysiological features of ureteral fibrosis and offers new insights into the coordinated behavior of multicellular ecosystems. Focusing on three major ECM components, Periostin, Collagen, and Laminin, and their respective integrin receptors (ITGA1, ITGA2, ITGB1, etc)., we mapped cross-cellular signaling modules. Multiple collagen subtypes were significantly upregulated in fibroblasts, while their integrin receptors were highly expressed in immune cells, epithelial cells, and pericytes. This collagen–integrin axis, initiated by fibroblasts, may facilitate structural remodeling, enhance cell adhesion, and provide a molecular scaffold for immune cell migration. Moreover, ECM–integrin interactions such as COL1A1–ITGAV/ITGB5 were particularly active between fibroblasts and ECs, suggesting a potential link between matrix remodeling and local angiogenesis. While such mechanisms have been reported in other fibrotic diseases,[64–66] their contribution to ureteral scar stricture remains largely unexplored, highlighting a promising direction for future research on vascular–stromal crosstalk in ureteral fibrosis.

In this study, we employed scRNA-seq to construct, for the first time, a comprehensive cellular lineage atlas of human ureteral scar stricture tissue, uncovering its intrinsic cellular heterogeneity and microenvironmental characteristics. Moreover, The enrichment of $S100A8^+$ and $MT1E^+$ basal epithelial cells, $APOE^+$ macrophages, and ECM-producing

fibroblasts with high periostin expression in scar tissue suggests that these features could serve as biomarkers for recurrence risk after surgical repair. Postoperative assessment of these markers—either through ureteral tissue biopsies or non-invasive approaches such as urine-derived exfoliated cell analysis—may help identify patients with a persistently activated fibrotic microenvironment who could benefit from closer surveillance or early adjuvant therapy. Nonetheless, several limitations should be acknowledged. First, the sample size was limited, and future studies involving larger patient cohorts are necessary to validate the generalizability of cell type-specific changes and associated signaling pathways. Second, the predicted intercellular interactions inferred from scRNA-seq data require confirmation through functional and mechanistic assays. Lastly, the lack of longitudinal sampling restricts our ability to assess the temporal dynamics of ureteral fibrosis. Future studies incorporating time-series analyses and spatial transcriptomics may offer deeper insights into the progressive remodeling of cellular phenotypes and microenvironmental crosstalk throughout disease progression.

Conclusion

This study is the first to utilize scRNA-seq to elucidate the extensive cellular heterogeneity and functional reprogramming underlying ureteral scar formation. Our findings reveal a profoundly altered microenvironment, characterized by complex and intensified communication networks among ECM-producing cells, immune populations, and structural lineages. These insights provide a robust conceptual framework and identify potential therapeutic targets to guide the development of precision interventions for ureteral fibrotic strictures.

Institutional Review Board Statement

All analyses performed involving human participants were in accordance with the ethical standards of the institutional and/or national research committee and with the 1964 Helsinki declaration and its later amendments or comparable ethical standards. This study was approved by the Ethics Committee of The First Affiliated Hospital of Anhui Medical University (Approval No. PJ 2025-02-92). Informed consent was obtained from all participants included in the study.

Acknowledgments

The author expresses gratitude for the valuable support and the beneficial discussions with other members of the urology, otolaryngology and infectious diseases departments.

Funding

This study is supported by the National Natural Science Foundation of China (82170787, 82370768, 82470800); The Natural Science Foundation of Anhui Province (2308085MH247).

Disclosure

The authors declare that they have no competing interests in this work.

References

1. Fröber R. Surgical anatomy of the ureter. *BJU Int*. 2007;100(4):949–965. doi:10.1111/j.1464-410X.2007.07207.x
2. Moretto S, Saita A, Scoffone CM, et al. Ureteral stricture rate after endoscopic treatments for urolithiasis and related risk factors: systematic review and meta-analysis. *World J Urol*. 2024;42(1):234. doi:10.1007/s00345-024-04933-2
3. Cohen KH, Teh BS, Paulino AC, Butler EB. Ureteral stenosis after postprostatectomy intensity-modulated radiotherapy. *Am J Clin Oncol*. 2010;33(1):108. doi:10.1097/COC.0b013e31802b30cb
4. Xu MY, Song ZY, Liang CZ. Robot-assisted repair of ureteral stricture. *J Robot Surg*. 2024;18(1):354. doi:10.1007/s11701-024-01993-9
5. Tyritzis SI, Wiklund NP. Ureteral strictures revisited…trying to see the light at the end of the tunnel: a comprehensive review. *J Endourol*. 2015;29(2):124–136. doi:10.1089/end.2014.0522
6. Cavalcanti AG, Costa WS, Baskin LS, McAninch JA, Sampaio FJ. A morphometric analysis of bulbar urethral strictures. *BJU Int*. 2007;100(2):397–402. doi:10.1111/j.1464-410X.2007.06904.x
7. Pohlers D, Brenmoehl J, Löffler I, et al. TGF-beta and fibrosis in different organs - molecular pathway imprints. *Biochim Biophys Acta*. 2009;1792(8):746–756. doi:10.1016/j.bbadis.2009.06.004
8. Abraham S. Editorial Comment to Myofibroblast-dominant proliferation associated with severe fibrosis in bulbar urethral strictures. *Int J Urol*. 2023;30(1):112–113. doi:10.1111/iju.15071

9. Rozen-Zvi B, Hayashida T, Hubchak SC, Hanna C, Platanias LC, Schnaper HW. TGF-β/Smad3 activates mammalian target of rapamycin complex-1 to promote collagen production by increasing HIF-1α expression. *Am J Physiol Renal Physiol*. 2013;305(4):F485–494. doi:10.1152/ajprenal.00215.2013
10. Hirano Y, Horiguchi A, Ojima K, et al. Myofibroblast-dominant proliferation associated with severe fibrosis in bulbar urethral strictures. *Int J Urol*. 2023;30(1):107–112. doi:10.1111/iju.15053
11. Andrews JP, Marttala J, Macarak E, Rosenbloom J, Uitto J. Keloids: the paradigm of skin fibrosis - Pathomechanisms and treatment. *Matrix Biol*. 2016;51:37–46. doi:10.1016/j.matbio.2016.01.013
12. Luecken MD, Theis FJ. Current best practices in single-cell RNA-seq analysis: a tutorial. *Mol Syst Biol*. 2019;15(6):e8746. doi:10.15252/msb.20188746
13. Stubbington M, Rozenblatt-Rosen O, Regev A, Teichmann SA. Single-cell transcriptomics to explore the immune system in health and disease. *Science*. 2017;358(6359):58–63. doi:10.1126/science.aan6828
14. Ramachandran P, Dobie R, Wilson-Kanamori JR, et al. Resolving the fibrotic niche of human liver cirrhosis at single-cell level. *Nature*. 2019;575(7783):512–518. doi:10.1038/s41586-019-1631-3
15. Psaila B, Wang G, Rodriguez-Meira A, et al. Single-Cell Analyses Reveal Megakaryocyte-Biased Hematopoiesis in Myelofibrosis and Identify Mutant Clone-Specific Targets. *Mol Cell*. 2020;78(3):477–492.e8. doi:10.1016/j.molcel.2020.04.008
16. Deng CC, Hu YF, Zhu DH, et al. Single-cell RNA-seq reveals fibroblast heterogeneity and increased mesenchymal fibroblasts in human fibrotic skin diseases. *Nat Commun*. 2021;12(1):3709. doi:10.1038/s41467-021-24110-y
17. Rudman-Melnick V, Adam M, Potter A, et al. Single-Cell Profiling of AKI in a Murine Model Reveals Novel Transcriptional Signatures, Profibrotic Phenotype, and Epithelial-to-Stromal Crosstalk. *J Am Soc Nephrol*. 2020;31(12):2793–2814. doi:10.1681/ASN.2020010052
18. Chen Z, Zhou L, Liu L, et al. Single-cell RNA sequencing highlights the role of inflammatory cancer-associated fibroblasts in bladder urothelial carcinoma. *Nat Commun*. 2020;11(1):5077. doi:10.1038/s41467-020-18916-5
19. Hirz T, Mei S, Sarkar H, et al. Dissecting the immune suppressive human prostate tumor microenvironment via integrated single-cell and spatial transcriptomic analyses. *Nat Commun*. 2023;14(1):663. doi:10.1038/s41467-023-36325-2
20. Zhang W, Zhang J, Jiao D, et al. Single-Cell RNA Sequencing Reveals a Unique Fibroblastic Subset and Immune Disorder in Lichen Sclerosus Urethral Stricture. *J Inflamm Res*. 2024;17:5327–5346. doi:10.2147/JIR.S466317
21. Zhang Q, Wang C, Qin M, et al. Investigating cellular similarities and differences between upper tract urothelial carcinoma and bladder urothelial carcinoma using single-cell sequencing. *Front Immunol*. 2024;15:1298087. doi:10.3389/fimmu.2024.1298087
22. Fink EE, Sona S, Tran U, et al. Single-cell and spatial mapping Identify cell types and signaling Networks in the human ureter. *Dev Cell*. 2022;57(15):1899–1916.e6. doi:10.1016/j.devcel.2022.07.004
23. Elyada E, Bolisetty M, Laise P, et al. Cross-Species Single-Cell Analysis of Pancreatic Ductal Adenocarcinoma Reveals Antigen-Presenting Cancer-Associated Fibroblasts. *Cancer Discov*. 2019;9(8):1102–1123. doi:10.1158/2159-8290.CD-19-0094
24. Lun A, Riesenfeld S, Andrews T, et al. EmptyDrops: distinguishing cells from empty droplets in droplet-based single-cell RNA sequencing data. *Genome Biol*. 2019;20(1):63. doi:10.1186/s13059-019-1662-y
25. Hao Y, Stuart T, Kowalski MH, et al. Dictionary learning for integrative, multimodal and scalable single-cell analysis. *Nat Biotechnol*. 2024;42(2):293–304. doi:10.1038/s41587-023-01767-y
26. Korsunsky I, Millard N, Fan J, et al. Fast, sensitive and accurate integration of single-cell data with Harmony. *Nat Methods*. 2019;16(12):1289–1296. doi:10.1038/s41592-019-0619-0
27. McGinnis CS, Murrow LM, Gartner ZJ. DoubletFinder: doublet Detection in Single-Cell RNA Sequencing Data Using Artificial Nearest Neighbors. *Cell Syst*. 2019;8(4):329–337.e4. doi:10.1016/j.cels.2019.03.003
28. Yang S, Corbett SE, Koga Y, et al. Decontamination of ambient RNA in single-cell RNA-seq with DecontX. *Genome Biol*. 2020;21(1):57. doi:10.1186/s13059-020-1950-6
29. Zhang H. *SCP: Single Cell Pipeline. R Package Version 0.5.6*. 2023.
30. Trapnell C, Cacchiarelli D, Grimsby J, et al. The dynamics and regulators of cell fate decisions are revealed by pseudotemporal ordering of single cells. *Nat Biotechnol*. 2014;32(4):381–386. doi:10.1038/nbt.2859
31. Kalluri R, Weinberg RA. The basics of epithelial-mesenchymal transition. *J Clin Invest*. 2009;119(6):1420–1428. doi:10.1172/JCI39104
32. Zwaans B, Carabulea AL, Bartolone SN, Ward EP, Chancellor MB, Lamb LE. Voiding defects in acute radiation cystitis driven by urothelial barrier defect through loss of E-cadherin, ZO-1 and Uroplakin III. *Sci Rep*. 2021;11(1):19277. doi:10.1038/s41598-021-98303-2
33. Jiang H, Shen J, Ran Z. Epithelial-mesenchymal transition in Crohn's disease. *Mucosal Immunol*. 2018;11(2):294–303. doi:10.1038/mi.2017.107
34. Jinde K, Nikolic-Paterson DJ, Huang XR, et al. Tubular phenotypic change in progressive tubulointerstitial fibrosis in human glomerulonephritis. *Am J Kidney Dis*. 2001;38(4):761–769. doi:10.1053/ajkd.2001.27693
35. Zeisberg M, Yang C, Martino M, et al. Fibroblasts derive from hepatocytes in liver fibrosis via epithelial to mesenchymal transition. *J Biol Chem*. 2007;282(32):23337–23347. doi:10.1074/jbc.M700194200
36. Marconi GD, Fonticoli L, Rajan TS, et al. Epithelial-Mesenchymal Transition (EMT): the Type-2 EMT in Wound Healing, Tissue Regeneration and Organ Fibrosis. *Cells*. 2021;10(7):1587. doi:10.3390/cells10071587
37. Wang J, Ding HK, Xu HJ, et al. Single-cell analysis revealing the metabolic landscape of prostate cancer. *Asian J Androl*. 2024;26(5):451–463. doi:10.4103/aja20243
38. Sisto M, Ribatti D, Lisi S. Organ Fibrosis and Autoimmunity: the Role of Inflammation in TGFβ-Dependent EMT. *Biomolecules*. 2021;11(2):310. doi:10.3390/biom11020310
39. Thulabandu V, Chen D, Atit RP. Dermal fibroblast in cutaneous development and healing. *Wiley Interdiscip Rev Dev Biol*. 2018;7(2). doi:10.1002/wdev.307
40. Ezzo M, Hinz B. Novel approaches to target fibroblast mechanotransduction in fibroproliferative diseases. *Pharmacol Ther*. 2023;250:108528. doi:10.1016/j.pharmthera.2023.108528
41. Ferreira BH, Silva IS, Mendes A, et al. Promoting ER stress in a plasmacytoid dendritic cell line drives fibroblast activation. *Cell Commun Signal*. 2025;23(1):66. doi:10.1186/s12964-025-02057-7
42. Tai Y, Woods EL, Dally J, et al. Myofibroblasts: function, Formation, and Scope of Molecular Therapies for Skin Fibrosis. *Biomolecules*. 2021;11(8):1095. doi:10.3390/biom11081095

43. Kisseleva T, Brenner D. Molecular and cellular mechanisms of liver fibrosis and its regression. *Nat Rev Gastroenterol Hepatol*. 2021;18(3):151–166. doi:10.1038/s41575-020-00372-7
44. Schuster R, Younesi F, Ezzo M, Hinz B. The Role of Myofibroblasts in Physiological and Pathological Tissue Repair. *Cold Spring Harb Perspect Biol*. 2023;15(1):a041231. doi:10.1101/cshperspect.a041231
45. Pakshir P, Hinz B. The big five in fibrosis: macrophages, myofibroblasts, matrix, mechanics, and miscommunication. *Matrix Biol*. 2018;68-69:81–93. doi:10.1016/j.matbio.2018.01.019
46. Meizlish ML, Franklin RA, Zhou X, Medzhitov R. Tissue Homeostasis and Inflammation. *Annu Rev Immunol*. 2021;39:557–581. doi:10.1146/annurev-immunol-061020-053734
47. Jin C, Zhang F, Luo H, et al. The CCL5/CCR5/SHP2 axis sustains Stat1 phosphorylation and activates NF-κB signaling promoting M1 macrophage polarization and exacerbating chronic prostatic inflammation. *Cell Commun Signal*. 2024;22(1):584. doi:10.1186/s12964-024-01943-w
48. Tacke F, Zimmermann HW. Macrophage heterogeneity in liver injury and fibrosis. *J Hepatol*. 2014;60(5):1090–1096. doi:10.1016/j.jhep.2013.12.025
49. Kishore A, Petrek M. Roles of Macrophage Polarization and Macrophage-Derived miRNAs in Pulmonary Fibrosis. *Front Immunol*. 2021;12:678457. doi:10.3389/fimmu.2021.678457
50. Pellicoro A, Ramachandran P, Iredale JP, Fallowfield JA. Liver fibrosis and repair: immune regulation of wound healing in a solid organ. *Nat Rev Immunol*. 2014;14(3):181–194. doi:10.1038/nri3623
51. Tang PM, Nikolic-Paterson DJ, Lan HY. Macrophages: versatile players in renal inflammation and fibrosis. *Nat Rev Nephrol*. 2019;15(3):144–158. doi:10.1038/s41581-019-0110-2
52. Shapouri-Moghaddam A, Mohammadian S, Vazini H, et al. Macrophage plasticity, polarization, and function in health and disease. *J Cell Physiol*. 2018;233(9):6425–6440. doi:10.1002/jcp.26429
53. Zhang M, Zhang S. T Cells in Fibrosis and Fibrotic Diseases. *Front Immunol*. 2020;11:1142. doi:10.3389/fimmu.2020.01142
54. Huang R, Wang W, Chen Z, et al. Identifying immune cell infiltration and effective diagnostic biomarkers in Crohn's disease by bioinformatics analysis. *Front Immunol*. 2023;14:1162473. doi:10.3389/fimmu.2023.1162473
55. Chen Y, Jin Q, Fu X, Qiao J, Niu F. Connection between T regulatory cell enrichment and collagen deposition in keloid. *Exp Cell Res*. 2019;383(2):111549. doi:10.1016/j.yexcr.2019.111549
56. Li Y, Liu H, Liang Y, Peng P, Ma X, Zhang X. DKK3 regulates cell proliferation, apoptosis and collagen synthesis in keloid fibroblasts via TGF-β1/Smad signaling pathway. *Biomed Pharmacother*. 2017;91:174–180. doi:10.1016/j.biopha.2017.03.044
57. Morante-Palacios O, Fondelli F, Ballestar E, Martínez-Cáceres EM. Tolerogenic Dendritic Cells in Autoimmunity and Inflammatory Diseases. *Trends Immunol*. 2021;42(1):59–75. doi:10.1016/j.it.2020.11.001
58. Farkas L, Horowitz JC, Mora AL. How a fibroblast ages: a role for bone morphogenetic protein 4 in protecting lung fibroblasts from senescence in pulmonary fibrosis. *Eur Respir J*. 2022;60(6):2201702. doi:10.1183/13993003.01702-2022
59. Livingston MJ, Shu S, Fan Y, et al. Tubular cells produce FGF2 via autophagy after acute kidney injury leading to fibroblast activation and renal fibrosis. *Autophagy*. 2023;19(1):256–277. doi:10.1080/15548627.2022.2072054
60. Rajasekaran D, Zierow S, Syed M, Bucala R, Bhandari V, Lolis EJ. Targeting distinct tautomerase sites of D-DT and MIF with a single molecule for inhibition of neutrophil lung recruitment. *FASEB J*. 2014;28(11):4961–4971. doi:10.1096/fj.14-256636
61. Florez-Sampedro L, Soto-Gamez A, Poelarends GJ, Melgert BN. The role of MIF in chronic lung diseases: looking beyond inflammation. *Am J Physiol Lung Cell Mol Physiol*. 2020;318(6):L1183–L1197. doi:10.1152/ajplung.00521.2019
62. Li L, Xiang T, Guo J, et al. Inhibition of ACSS2-mediated histone crotonylation alleviates kidney fibrosis via IL-1β-dependent macrophage activation and tubular cell senescence. *Nat Commun*. 2024;15(1):3200. doi:10.1038/s41467-024-47315-3
63. Larson-Casey JL, Deshane JS, Ryan AJ, Thannickal VJ, Carter AB. Macrophage Akt1 Kinase-Mediated Mitophagy Modulates Apoptosis Resistance and Pulmonary Fibrosis. *Immunity*. 2016;44(3):582–596. doi:10.1016/j.immuni.2016.01.001
64. Shim J, Oh SJ, Yeo E, et al. Integrated Analysis of Single-Cell and Spatial Transcriptomics in Keloids: highlights on Fibrovascular Interactions in Keloid Pathogenesis. *J Invest Dermatol*. 2022;142(8):2128–2139.e11. doi:10.1016/j.jid.2022.01.017
65. Kanchanawong P, Calderwood DA. Organization, dynamics and mechanoregulation of integrin-mediated cell-ECM adhesions. *Nat Rev Mol Cell Biol*. 2023;24(2):142–161. doi:10.1038/s41580-022-00531-5
66. Cao Y, Su H, Zeng J, et al. Integrin β8 prevents pericyte-myofibroblast transition and renal fibrosis through inhibiting the TGF-β1/TGFBR1/Smad3 pathway in diabetic kidney disease. *Transl Res*. 2024;265:36–50. doi:10.1016/j.trsl.2023.10.007